Wide-Area Imaging of Ultrasonic Lamb Wave Fields by Electronic Speckle Pattern Interferometry

Grant A. Gordon and T. Douglas Mast

Applied Research Laboratory, The Pennsylvania State University
P.O. Box 30, State College, PA 16804

ABSTRACT

Ultrasonic elastic waves have traditionally been examined using single point measurement techniques. In this paper, we present a technique capable of recording out-of-plane ultrasonic displacement data over wide areas. The method employs two-dimensional surface vibration data collected via electronic speckle pattern interferometry used in combination with laser modulation and optical phase stepping. Using this rapid, wide-area measurement method, images of ultrasonic Lamb waves on ideal and flawed plate structures are presented. For a single ultrasonic excitation frequency, multiple data records are collected as an externally excited traveling plate wave moves through the sample. When an optical phase shift is introduced between the data records, the data can be processed to yield quantitative displacement fields. The resulting processed images demonstrate evidence of Lamb wave reflection, transmission and scattering. Following the full field data collection, a novel inverse scattering algorithm was applied to reconstruct images of the scattering sources responsible for the measured displacement field data. The results of these investigations will be presented and discussed in the context of detecting hidden flaws in aging aircraft.

Keywords: Phase-stepping, ESPI, Holography, Non-destructive Evaluation (NDE), and Inverse Scattering.

1. INTRODUCTION

1.1. Optical Detection of Ultrasound

The optical detection of ultrasound has been an active area of research for many years. As discussed in various text books and review articles[1-3], there are a number of techniques for sensing displacements at the free surface of an object when the amplitude of displacement is less than the optical wavelength of the probing light. Many of the techniques are primarily suited to studying a single point on the surface sample since the displacement is sensed with a focused or collimated beam. To provide images of an area, the probing beam can be raster scanned over the region of interest. Naturally, this added sophistication extracts a penalty in terms of inspection system cost, speed and complexity. Thus this approach has seen only limited application, primarily in the area of transducer calibration,[4-6] although progress has also been reported in the area of laser based inspection of aircraft parts. J-P. Monchalin et al.[7,8] describe the use of a scanned confocal Fabry-Perot interferometer to generate C-scan images of CF-18 fuselage, wings and stabilizers and other composite parts.

Full field ultrasonic displacement imaging techniques have also been applied primarily to the problem of transducer characterization using the double exposure holographic interferometry[3,5,9] and Schlieren[10] approaches. However there have been some limited reports on the use of full field techniques to study ultrasonic surface waves and plate (Lamb) waves. J. Wagner[11,12] described a heterodyned holographic system for visualizing a traveling surface acoustic wavefront. K.-J. Pohl et al.[13] described a pulsed holographic system for imaging laser generated Rayleigh waves. C. Henning and D. Mewes[14] used double pulsed holographic interferometry to visualize ultrasonic surface waves traveling over surfaces eroded by particle impact. Similarly, the use of speckle interferometry techniques for measuring wide area ultrasonic surface

Further author information --
G. A. Gordon: Email: gag100@psu.edu Tel: (814) 863-0896
T. D. Mast: Email: mast@sabine.acs.psu.edu Tel: (814) 863-9998

Part of the SPIE Conference on Nondestructive Evaluation of Aging Aircraft, Airports, and Aerospace Hardware III • Newport Beach, California • March 1999
SPIE Vol. 3586 • 0277-786X/99/$10.00

and plate waves has rarely been reported. The principal reason for this dearth of activity is the limited detection sensitivity provided by full field techniques.

Speckle interferometry techniques are very similar to holographic techniques with one significant difference. Speckle interferometry methods do not produce an intermediate hologram but record the speckle patterns directly on a low resolution recording medium[15] unsuitable for holographic reconstruction. For example, electronic speckle pattern interferometry (ESPI), also known as TV holography, records the speckle data with a TV or CCD camera. By eliminating the rate-limiting holographic reconstruction step, ESPI systems can be designed to electronically process the data and provide near real time wide area displacement measurements. In the present paper, we describe an ESPI method combined with laser modulation and optical phase stepping capable of imaging ultrasonic Lamb wave fields at near real time rates. In addition to the TV holography approach, Gordon et al.[16] and Bard et al.[17] have described a method for imaging ultrasonic surface waves by another ESPI technique known as digital phase stepping shearography (DPSS). Recently this technique has been used to image plate waves,[16-18] bar modes,[16,17] scattered Lamb waves generated from defects in aluminum plates,[16] as well as defects in C/epoxy plates.[18] Although the DPSS method has a number of advantages over the present ESPI technique, including tolerance to rigid body motion, and reduced laser coherence requirements, the present ESPI approach was adopted in this study because it provides a more direct measurement of the Lamb wave displacement field. This simplification was a key point to consider as we sought to develop our flaw image reconstruction algorithm.

1.2. A Promising NDE Approach for Aging Aircraft

Concern about mechanical safety is growing as the median age of active commercial and military aircraft increases. In the civilian aircraft industry, tragedies including the Aloha Airline 737 fuselage failure and the United Airlines DC-10 engine breakdown have led the FAA, in cooperation with other government organizations, to fund a comprehensive and coordinated program on the nondestructive inspection of aging aircraft since 1990. Despite recent activities, many in the commercial aviation community believe that few, if any, of the existing inspection requirements can be addressed by the current and emerging wide area inspection systems.[19] Yet, it is anticipated that rapid imaging inspection will be the next substantial change in airplane inspection practice. The ideal next generation inspection system would provide quantitative flaw characterization, allow detection of small cracks even in multilayer structures, and establish a precise and reproducible correspondence between indication and flaw.[20]

One approach to this problem is to detect defects from the scattered, reflected and transmitted response of transient high frequency Lamb waves interacting with airframe defects and surrounding structures. When elastic waves are generated on a plate or shell-like structure, areas of inhomogeneity such as disbonds, cracks, and delaminations cause reflection, scattering, mode conversion, and other complex wave effects. Recently, a number of researchers have examined the use of Lamb waves for nondestructive testing. Although this area of aircraft inspection is fairly new, current results strongly suggest that Lamb wave interrogation has the potential to detect hidden flaws in aging aircraft.[21-25] Despite the fact that the mechanics of elastic wave propagation in a multi-layered solid have been known for some time, theoretical and experimental work on the application of guided Lamb waves for nondestructive evaluation of defects has not been extensive. Some researchers, such as Gordon and Tittmann,[26,27] have investigated the use of guided waves and guided wave dispersion for material characterization, but investigations into the scattering of guided Lamb waves from defects is particularly sparse. Lamb wave reflections from a free edge have been studied by Torvik,[28] and later by Gregory and Gladwell.[29] Rokhlin has reported on the use of Lamb waves to detect elongated delaminations,[30] and on the interaction of Lamb waves with spot welds.[31] The problem of Lamb wave interaction with defects has also been tackled by numerical methods such as, finite element techniques,[25,32] and boundary element techniques.[33] Notwithstanding these efforts, the practical application of Lamb wave methods to aircraft is a complicated problem that still awaits a complete solution.

In real aircraft structures, scattered, reflected, and transmitted ultrasonic fields can form a very complicated pattern due to complex combinations of rivets, ribs, backing straps, bulkheads, and other components. This complexity places severe limitations on the applicability of techniques employing single ultrasonic transmitters and receivers. In contrast, ESPI techniques can obtain *broad-band spatial frequency* information, which provides a quantitative visualization of the full ultrasonic wavefield after only one measurement. The noncontact nature of the data collection means that images can be obtained and combined without concern for the distorting effects of coupling inconsistencies. Generally it is not a simple task to separate the measured scattered wavefield due to the flaws from the complicated wavefield generated by the

interaction of the ultrasound with the normal structure. To detect flaws in such a situation, a more complete approach is needed to reconstruct the underlying structure from the measured wavefield. One possible method for quantitative flaw characterization in plate structures is that of Lamb wave tomography.[34-36] This technique has been used to image flaws but possesses weaknesses characteristic of its algorithm. For example, multiple measurements are required to construct a data set for the inversion process, and the resolution depends on the number of independent measurements and their orientation. Furthermore, the commonly used filtered backprojection algorithms are limited since they neglect scattering effects and assume straight, unperturbed propagation paths for the elastic energy.

This paper presents a new approach to the interpretation of scattered ultrasonic waves in plate structures. Starting from ultrasonic wavefields measured by ESPI techniques, quantitative reconstruction of scattering sources from a single two-dimensional image of the scattered wavefield can be used to detect and quantify subsurface flaws. The present investigation employs a TV holography approach combined with laser modulation and optical phase stepping. When a shearography configuration is employed, rapid, vibration immune, wide-area sensing can be achieved over rough and curved surfaces. Recently a portable digital phase-stepping shearography (DPSS) system has been demonstrated for inspection of aircraft components under *static* loading conditions. In particular, the system was used to successfully conduct field demonstrations at the North Island Naval Air Station at San Diego on the FA-18 horizontal stabilizer and aileron.[37] We anticipate that the lessons learned in the present investigation will be transferable to the portable DPSS, providing a new and promising approach to aging aircraft inspection.

2. EXPERIMENTAL METHODS: LAMB WAVE DETECTION

The modified ESPI system used to collect the data is shown in Figure 1. A Pulnix 960x680 pixel CCD camera is located at the image plane of the speckle interferometer where it can record the interference pattern formed when two coherent speckle wavefronts combine. Given complex amplitudes for the two wavefronts as $U_1 = u_1 \exp(i\Phi_1)$ and $U_2 = u_2 \exp(i\Phi_2)$, the intensity I of any given point (x,y) in the image plane can be described as

$$I = I_1 + I_2 + 2\sqrt{I_1 I_2}\cos\phi \tag{1}$$

where I_1 is $U_1 U_1^*$, I_2 is $U_2 U_2^*$, and $\phi = \Phi_1 - \Phi_2$, the relative phase between the two wavefronts. In this expression the term $(I_1 + I_2)$ is often referred to as the background intensity, while the $2(I_1 I_2)^{1/2}$ term is called the fringe modulation intensity. After this intensity data has been electronically stored, the object can be displaced. The new intensity distribution is then given as

$$\underline{I} = I_1 + I_2 + 2\sqrt{I_1 I_2}\cos(\phi + \Delta\phi) \tag{2}$$

It is common in ESPI to electronically subtract the stored image from the new image displaying the difference between the two speckle patterns. The resulting image produces a fringe pattern corresponding to the deformation field. However, more complete information can be obtained by a phase stepping technique. In this method, a series of optically phase shifted images are captured for each of the two object states. From these images, the phase at all points in the field of both images can be calculated. Unlike standard subtraction fringe patterns, this phase stepping approach allows displacement direction to be recovered and measurement depth resolution is increased by at least two orders of magnitude. This high sensitivity arises due to the coherent processing of the multiple images. After processing, the composite image can have a displacement resolution up to 1/1000 of an optical wavelength, while the standard fringe pattern resolution is only half an optical wavelength. The signal-to-noise ratio (SNR), realized by the visual contrast of the resulting phase map pattern, is also increased substantially over the fringe pattern techniques.

In our method, a four phase step algorithm is used since this provides a good combination of computational efficiency and signal to noise improvements.[38] The four optical path length increases of 0, $\pi/2$, π, and $3\pi/2$ are produced by driving the PZT stack mounted mirror to predetermined positions. This has the effect of generating four speckle images with intensities given by

$$I = I_1 + I_2 + 2\sqrt{I_1 I_2}\cos(\phi) \tag{3}$$

$$I^{\pi/2} = I_1 + I_2 + 2\sqrt{I_1 I_2}\cos(\phi + \pi/2) \tag{4}$$

$$I^{\pi} = I_1 + I_2 + 2\sqrt{I_1 I_2}\cos(\phi + \pi) \tag{5}$$

$$I^{3\pi/2} = I_1 + I_2 + 2\sqrt{I_1 I_2}\cos(\phi + 3\pi/2) \tag{6}$$

The phase distribution $\phi(x, y)$ can then be calculated by the expression

$$\phi = \tan^{-1}\frac{I^{3\pi/2} - I^{\pi/2}}{I - I^{\pi}} \tag{7}$$

Accordingly, the phase distribution for the displaced object can be obtained in the same way:

$$\phi + \Delta\phi = \tan^{-1}\frac{\underline{I}^{3\pi/2} - \underline{I}^{\pi/2}}{\underline{I} - \underline{I}^{\pi}} \tag{8}$$

The phase difference between the two object positions is then obtained by subtracting Eq. (7) from Eq. (8):

$$\Delta\phi(x, y) = \tan^{-1}\frac{I^{3\pi/2} - I^{\pi/2}}{I - I^{\pi}} - \tan^{-1}\frac{\underline{I}^{3\pi/2} - \underline{I}^{\pi/2}}{\underline{I} - \underline{I}^{\pi}} \tag{9}$$

For the geometry under consideration, the phase quantity of Eq. (9) is a direct measure of the surface normal displacement, **d**, between the two states

$$\Delta\phi = \frac{2\pi}{\lambda}(\mathbf{n}_0 - \mathbf{n}_1)\cdot\mathbf{d} \tag{10}$$

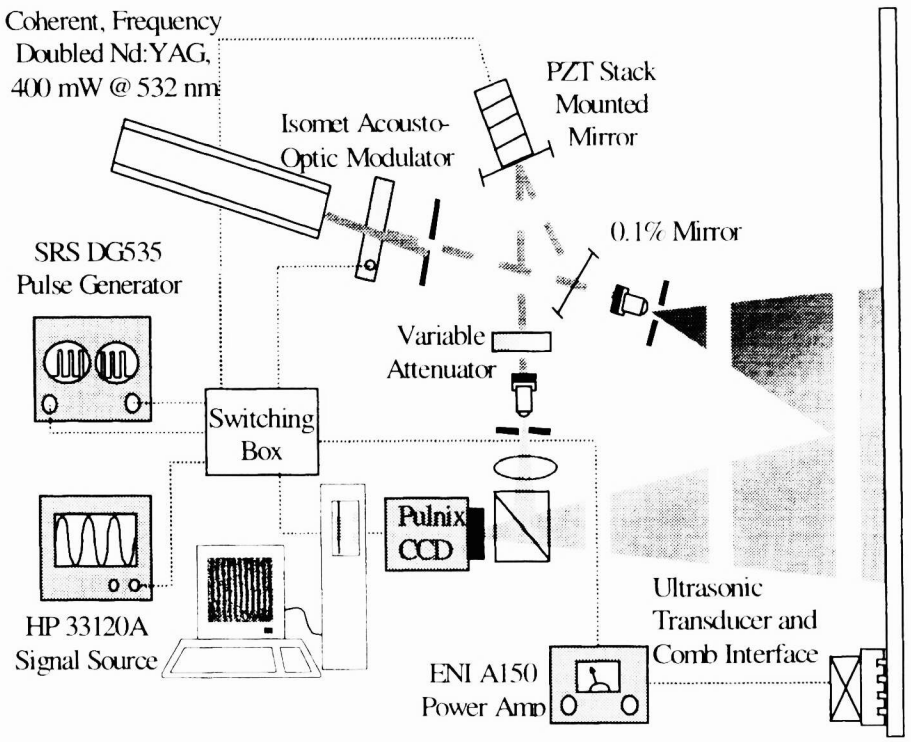

Figure 1. Schematic diagram of the experimental setup.

where $\mathbf{n}_0$ is the illumination direction and $\mathbf{n}_s$ is the viewing direction. When the viewing and illumination directions are normal to the surface, the system is geometrically optimized for measuring out-of-plane displacements. In practice it is often difficult to fulfill the normal direction criterion. However, when the departure from the normal condition is small, a good approximation to Eq. (10) is given as[39]

$$\Delta\phi = \frac{2\pi d}{\lambda}(\cos\theta_0 + \cos\theta_s) \tag{11}$$

where θ_0 and θ_s are the angles between the illumination direction and the viewing direction with respect to the surface normal respectively.

In addition to phase stepping, there is another significant departure from a standard ESPI configuration shown in our experimental setup. To capture traveling Lamb waves we have combined the digital phase stepping ESPI system with laser modulation. By driving an acousto-optic modulator with a pulse sequence synchronized to the driving source, the transmitted laser light 'stroboscopically' freezes the motion of the sample in a single displacement distribution. Since the final data, $\Delta\phi$, gives the phase difference between two displacement conditions, we can maximize the data SNR by ensuring that the two sample states have displacements that are large and opposite in direction. For traveling ultrasonic wavefields, driven at a single frequency, this criteria is established when the *I* and *I* conditions are stroboscopically frozen 180 degrees out of phase from each other. To employ phase stepping and real time data display in harmony with the stroboscopic illumination the timing sequence of these events must be coordinated. This was achieved by synchronizing the drive signal and acousto-optic modulator, which were in turn controlled according to the data acquisition rates established by the computer, through a switching box. Figure 2 shows the timing relationship between the various operations. In the interest of clarity the drive signal and laser modulation signal are shown at a frequency significantly slower that those used for data collection.

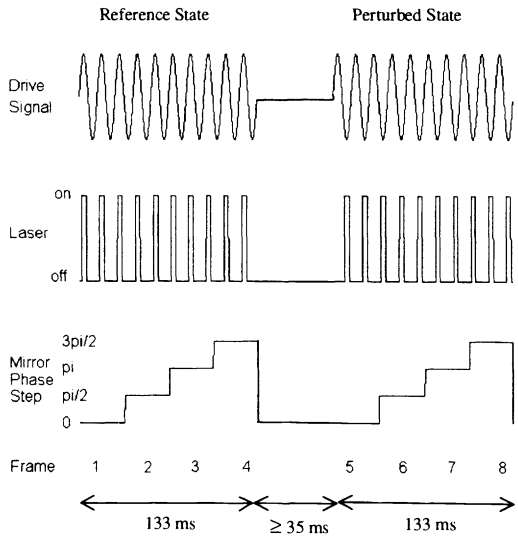

Figure 2. Timing diagram used to control the signal source, acousto-optic modulator, PZT stack and camera.

3. EXPERIMENTAL METHODS: LAMB WAVE GENERATION

The wavefield image quality improves as the signal to noise of the collected data is increased. In addition to steps taken to enhance the data collection performance of the system, we considered signal generation aspects as well. The ability to generate large amplitude Lamb waves is an important step towards enhancing system signal to noise. There are a number of

ways to generate ultrasonic Lamb waves on plates by both contact and non-contact means. Despite the appeal of non-contact excitation, the added complexity is not always warranted. In a simpler approach, we used a classical but less common technique for generating Lamb waves, the comb-structure method. As described by Viktorov,[40] a set of normal perturbations, such as an array of line contacts, can be an efficient source for generating Rayleigh or Lamb waves. In fact, Viktorov found that a properly designed comb structure driven by a bonded X-cut quartz crystal was a more efficient Rayleigh wave generator than the use of a polystyrene wedge, a directly bonded Y-cut quartz crystal, or a directly bonded X-cut quartz crystal. For simplicity, we chose to optimize the generation of a single Lamb wave mode, the fundamental antisymmetric mode, A_0. To avoid stimulating higher order modes, we drove the transducer below the cut-off frequency of the next higher order mode. This criterion is met if the driving frequency is maintained below the cut-off frequency, f_c, for the A_1 mode. This frequency can be determined from the relation $f_c=c_t/2d$, where d is the plate thickness and c_t is the bulk shear wave velocity for the plate material. Substituting values for an 1/8" (3.2mm) aluminum plate with $c_t \sim 3.0$ mm/us we find f_c is 470 kHz.

The comb structure method consists of generating a set of normal perturbations on the surface of the sample with a spatial periodicity equal to the wavelength of the desired Lamb wave mode. Figure 3 shows a plot of wavelength versus frequency for the fundamental Lamb wave modes on a 1/8" aluminum plate determined from the Rayleigh-Lamb frequency equation for propagation in an isotropic plate. Notice that the spatial frequency (wavelength) required to generate a S_0 mode is significantly different that the spatial frequency required for A_0 mode genertion. This plot does not show the nature of the particle motion. The displacement for the A_0 mode at the plate surface is primarily out-of-the-plane. This avails the A_0 mode to generation through the spatial distribution of normal forces provided by the comb structure. However, this is not true of the S_0 mode which is difficult to generate by a distribution of normal displacements at the surface (at these frequencies and plate thickness values).

F. L. Degertekin and B. T. Khuri-Yakub[41] have studied the relative efficiency of exciting an S_0 mode or an A_0 mode from a single normal point force. Their results show that the efficiency of generating of an A_0, for the thickness and frequencies used in our experiment, is approximately 35 dB larger than for the S_0 mode. The relative efficiencies of generation and the differences in spatial frequency virtually assure that only one mode of excitation is generated by the comb structure. Figure 3 also illustrates how the sensitivity to flaw size can be increased as the frequency is increased. However there is a trade-off. From fundamental analysis, the displacement at the end of a clamped piezoelectric bar driven at resonance is given by

$$\xi = -j\frac{\beta e}{\omega Z_{in}} \tag{12}$$

where β is a transformation factor related to geometry and material properties, e is driving voltage, Z_{in} is the total input impedance seen by the driving electrical circuit and ω is the angular frequency. To a first order approximation we can see that for transducers of similar size and properties, but different resonant frequencies, the displacement of the lower frequency source will be larger than for the higher frequency source in proportion to ω. This has a direct impact on the data SNR.

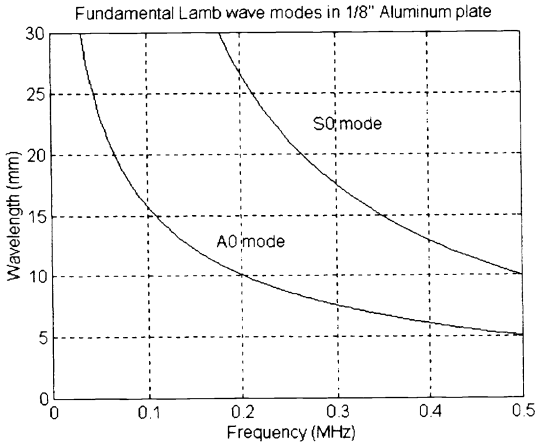

Figure 3. Wavelength versus frequency for an A_0 Lamb wave mode on a 1/8" aluminum plate.

4. IMAGING RESULTS

ESPI data was collected from an 1/8" aluminum plate supported at its ends and surrounded by a bead of modeling clay to absorb waves incident on the plate extremities. Figure 4 shows a photograph of the sample prior to data collection. Both the transducer used to generate the incident A_0 waves and the clay used as a damping material can seen in the figure. Also, the position where defects were intentionally cut into the underside of the plate are shown with the aid of surface mounted paper. These two defects, a cross pattern and a circular hole of diameter 3/16" (~ 5 mm), are not visible from the front side of the plate when the indication paper is removed prior to data collection. The detailed dimensions of the large flaw are shown in Figure 5. Figure 6 shows a displacement map generated from the collected and processed ESPI data before any defects were introduced to the plate. The 1-3 composite transducer was driven at 220 kHz.

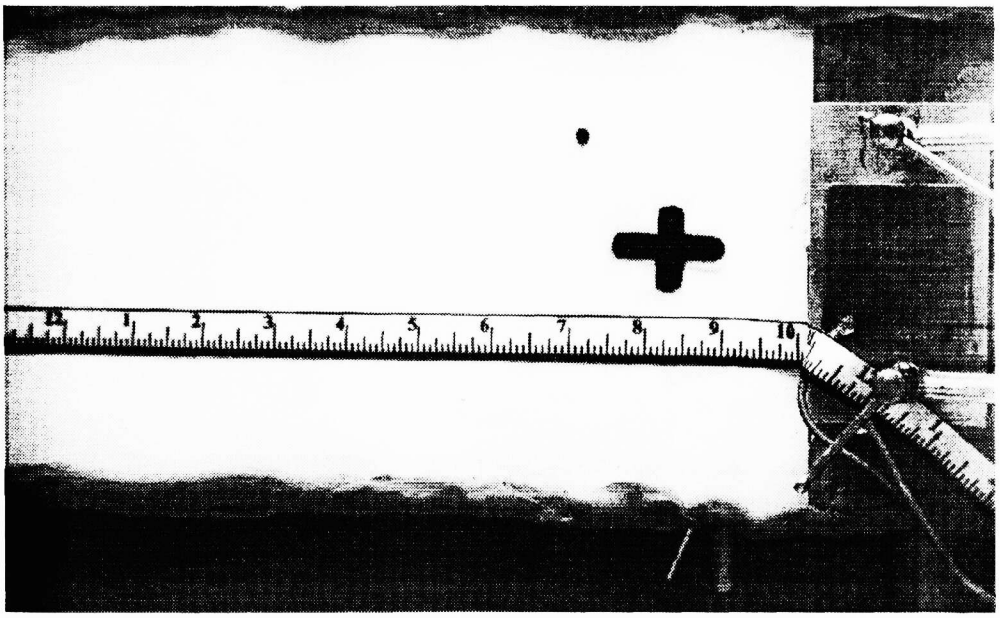

Figure 4. A white light image of the sample before ESPI data collection. Both the transducer used to generate the incident A_0 waves and the clay used as a damping material can seen. The position where defects where intentionally cut into the underside of the plate are shown with the aid of surface mounted paper. This paper is removed prior to data collection.

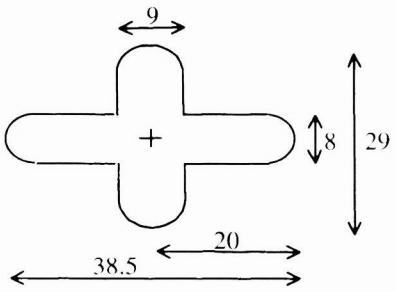

Figure 5. Dimensions of the intentional cross pattern defect machined 2 mm deep into the plate. All dimensions are in millimeters.

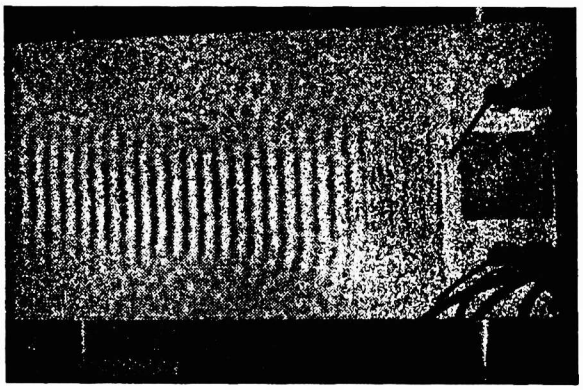

Figure 6. Processed EPSI data showing an A_0 plane waves traveling on the undamped plate before flaws were introduced.

Figure 7 and Figure 8 show the displacement fields that result when the generated A_0 waves interact with the flaws intentionally machined into the back of the plate. The incident A_0 waves were generated by a 1-3 composite transducer driven at 230 kHz while mounted on a comb structure with fingers separated by a spatial period of approximately 10 mm.

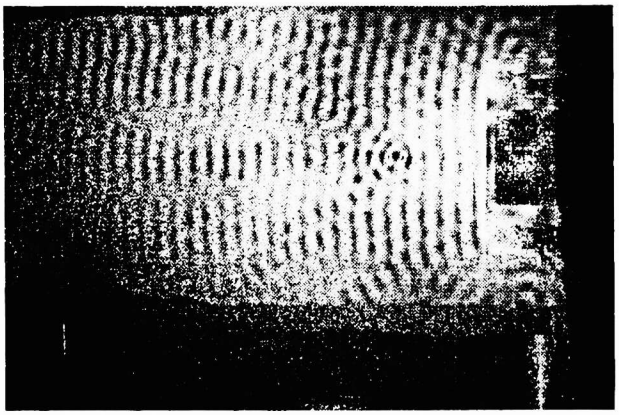

Figure 7. Displacement field image showing an A_0 plane waves interacting with the hidden but intentionally fabricated flaws. The incident plane wave was driven from the end of the plate.

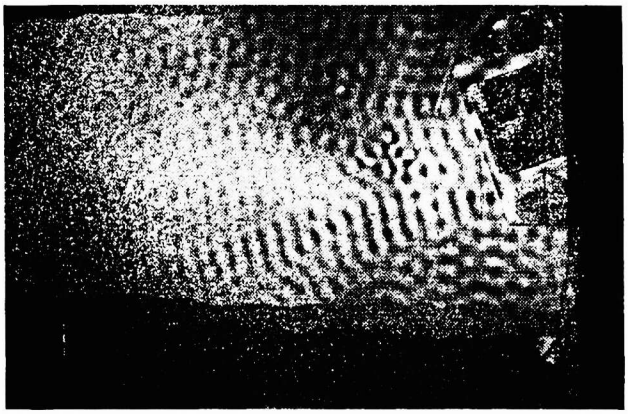

Figure 8. Displacement field image showing an A_0 plane wave interacting with the hidden but intentionally fabricated flaws. The incident plane wave was driven from the top right hand corner of the plate.

5. RECONSTRUCTION METHOD

To image flaws and other inhomogeneities, a technique has been developed to reconstruct effective scattering sources within the measured wavefields. Only one out-of-plane displacement map is required as input to the algorithm. The method starts by representing the calculated wavefield as a convolution between an assumed Green's function and an unknown distribution of effective scattering sources. These sources are taken to be directly proportional to the flaw contrast based on the assumptions that: i) the flaw causes a local variation in the Lamb wave propagation speed, ii) absorption effects are small, and iii) only one Lamb wave mode needs to be considered. Under these assumptions, the complete wavefield, $u(\mathbf{r})$, obeys the integral equation[42]

$$u(\mathbf{r}) = G(k_0,\mathbf{r}) \otimes \left(Q(\mathbf{r}) - k_0^2 u(\mathbf{r})\gamma(\mathbf{r})\right) \tag{13}$$

where $\otimes$ represents a two-dimensional spatial convolution, $Q(\mathbf{r})$ is a distribution of real acoustic sources associated with the driving transducer, and k_0 is the wavenumber for propagation in the absence of flaws. In addition, G denotes the Green's function for the Helmholtz equation in an unbounded two-dimensional medium, defined in terms of the Hankel function H_0 as

$$G(k_0,\mathbf{r}) = \frac{i}{4} H_0(k_0,\mathbf{r}) \tag{14}$$

and $\gamma(\mathbf{r})$ is the contrast associated with wavespeed variations, given by

$$\gamma(\mathbf{r}) = \frac{c_0^2}{c(\mathbf{r})^2} - 1 \tag{15}$$

From Eq. (13) we see that the total ultrasonic wavefield results from both a real source distribution, $Q(\mathbf{r})$, and an effective source distribution, $-k_0^2 u(\mathbf{r})\gamma(\mathbf{r})$. This effective source distribution, associated with scattering effects, results from interaction between the wavefield $u(\mathbf{r})$ and the wavespeed inhomogeneities described by $\gamma(\mathbf{r})$.

Equation (13) can be used as a starting point for methods of quantitatively reconstructing the contrast function $\gamma(\mathbf{r})$ from measurements of the wavefield $u(\mathbf{r})$. Regions of nonzero contrast correspond either to flaws or to known inhomogeneities such as rivets and rib structures. The inverse scattering problem of determining $\gamma(\mathbf{r})$ from $u(\mathbf{r})$ is nonlinear in nature because the wavefield $u(\mathbf{r})$ is itself a function of $\gamma(\mathbf{r})$. Thus, reconstructions of strongly scattering contrast functions are not easily obtained from conventional scattering measurements in which $u(\mathbf{r})$ is measured at a number of discrete points.[43-45] However, full-field measurement of the total ultrasonic wavefield, $u(\mathbf{r})$, allows direct inversion of Eq. (13) to image the effective source term $u(\mathbf{r})\gamma(\mathbf{r})$ for a large class of contrast functions.

This method for imaging the flaw distribution is shown diagramatically in Fig. 9. The first step is to generate a traveling Lamb wave in the sample by driving the transducer-comb-filter combination with a tone burst signal. Then the resulting out-of-plane displacement associated with reflection, transmission and scattering of the ultrasonic Lamb waves is measured using the modified ESPI system. After data processing to provide the out-of-plane displacement fields, a region of interest containing no real ultrasonic sources is selected for analysis. Filtering and/or averaging is performed on the displacement field to reduce optical speckle artifacts. Next, Hilbert transforms are applied to consecutive one-dimensional slices of the displacement field along the principal direction of propagation. This yields an estimate of the complex wavefield $u(\mathbf{r})$. The spatial-frequency content of this complex wavefield is analyzed to determine the wavenumber k_0 associated with the incident wave. Both the complex wavefield and the Green's function are windowed by a two-dimensional Blackman window before Fourier transformation. They are then spatially Fourier transformed to obtain the wavespace representations $\mathfrak{u}(\mathbf{k})$ and $\mathfrak{G}(k_0,\mathbf{k})$. Finally, a filtered deconvolution of Eq. (13) is performed using the formula:

$$u(\mathbf{r})\gamma(\mathbf{r}) = \frac{1}{k_0^2}\mathfrak{F}^{-1}\left(\frac{\mathfrak{u}(\mathbf{k})\Phi(\mathbf{k})}{\mathfrak{G}(k_0,\mathbf{k}) + \varepsilon\|\mathfrak{G}\|}\right) \tag{16}$$

Equation (16) yields a quantitative image of the effective scattering source, $u(\mathbf{r})\gamma(\mathbf{r})$. In this equation, $\mathfrak{F}^{-1}$ represents a two-dimesional inverse Fourier transform, $\Phi(\mathbf{k})$ is a spatial-frequency filter applied to ensure stability of the inversion, ε is a small regularization parameter, and $\|\mathfrak{G}\|$ is the L^2 norm of $\mathfrak{G}$. Using FFT algorithms to compute the Fourier transforms appearing in the above deconvolution, quantitative images can be computed very efficiently. The imaged quantity $u(\mathbf{r})\gamma(\mathbf{r})$ is directly proportional to the contrast, so that there exists a one-to-one correspondence between imaged "hot spots" and structural inhomogeneities such as flaws. When fused with an optical image of the structure surface, this image can be used to directly identify and characterize flaws in relation to normal structure.

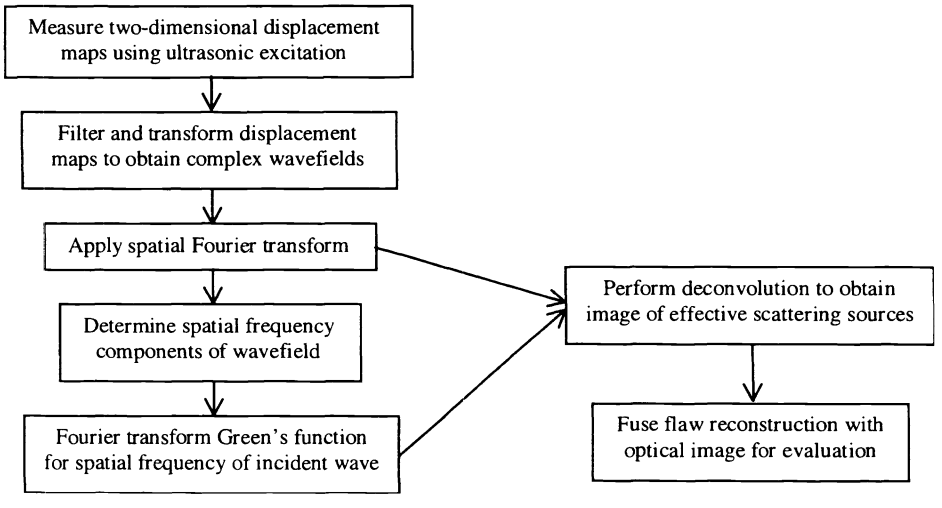

Figure 9. Flow diagram of full-field ultrasonic imaging method.

6. RECONSTRUCTION RESULTS

The reconstruction method described above has been applied to both simulated and experimentally measured data. The simulated data was derived for two different scattering inhomogeneities, a circular flaw and a discretized Sierpinski triangle.. In the circle simulations, an exact solution for scattering from a circular flaw of variable wavespeed was used to generated the scattering data assuming an incident plane wave, $\exp(ik_0x)$.[42] The real part of the wavefield was computed on a 256x256 grid with width dimensions equal to four times the radius of the circle. For the Sierpinski triangle simulation, the scattering data was generated using a finite-difference time-domain (FDTD) method.[46,47] This approach yields the total wavefield for arbitrarily shaped flaws. In this simulation, the incident wavefield was produced by a point source, realized by applying a sinusoidal displacement variation at one grid point.

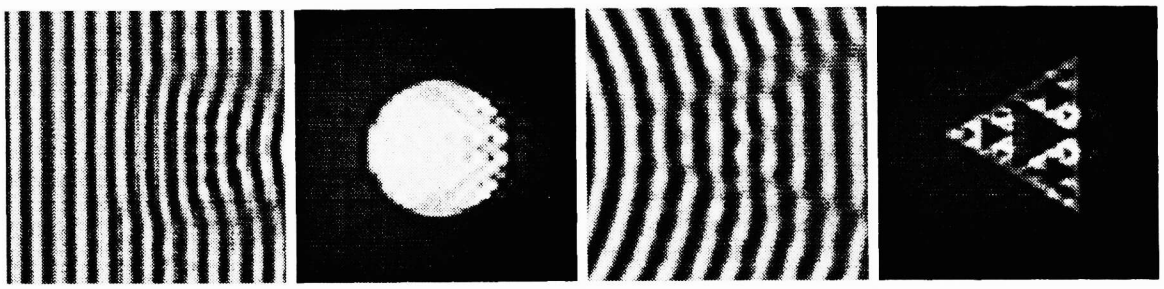

Figure 10. Simulated reconstruction of flaws from full-wave ultrasonic data. In each case, the reconstruction was obtained from the wavefield shown using the proposed quantitative imaging method. Left to right: (a) Wavefield caused by a circular flaw, contrast γ=0.2. (b) Reconstruction of the circular flaw. (c) Wavefield caused by a Sierpinski triangle flaw, contrast γ=0.4. (d) Reconstruction of the Sierpinski triangle flaw.

The simulated wavefields, as well as the reconstructed effective source distributions, are shown in Figure 10 for both simulations. The portion of the wavefield shown has only half the height and width used in the reconstruction. Notice that the reconstruction for the simulated circular flaw clearly resolves the flaw edges with high contrast. The Sierpinski triangle reconstruction shows resolution of inner triangles of dimensions much smaller than the central wavelength. This result demonstrates the capability of the reconstruction method to achieve resolution beyond the Rayleigh resolution limit and suggests that evanescent wave information is exploited.

A flaw reconstruction from the experimental ESPI data is shown in Fig. 11. The wavefield data used for the reconstructions were generated using the transducer-comb-filter combination driven by tone burst of 253 kHz. Data were collected for two different orientations of the source on the plate. Before reconstructions were performed, six measured wavefields for the source pointing along the long axis were averaged. Similarly, five measured wavefields for the source pointed across the long axis were averaged. This averaging step was taken in order to reduce image speckle. Each of the two averaged wavefields was used as input data for the reconstruction algorithm, with a central wavenumber determined from a spatial-frequency calculation. Blackman windowing was used in real space over the entire region of interest. Low-pass filtering was performed in wavespace using Blackman windows with spatial-frequency cutoffs designed to provide good resolution while minimizing the effects of optical speckle noise. The reconstruction shown was generated by combining two separate reconstructions, one for each source location.

7. SUMMARY

An ESPI technique capable of recording out-of-plane ultrasonic displacement data over wide areas has been described. Using this rapid, wide-area measurement method, images of ultrasonic Lamb waves on ideal and flawed plate structures were collected and presented. The resulting processed images demonstrate evidence of Lamb wave reflection, transmission and

:attering due to flaws. A novel inverse scattering algorithm was applied to reconstruct images of effective scattering sources om displacement field data. Reconstruction results, both for synthetic data and for ESPI displacement data, show that flaws ın be imaged with resolution suitable for nondestructive testing. The results of these investigations illustrate that a wide-·ea ESPI Lamb-wave imaging system, augmented by a new method for reconstruction of effective scattering sources ssociated with flaws, could be a valuable tool for aging aircraft inspection.

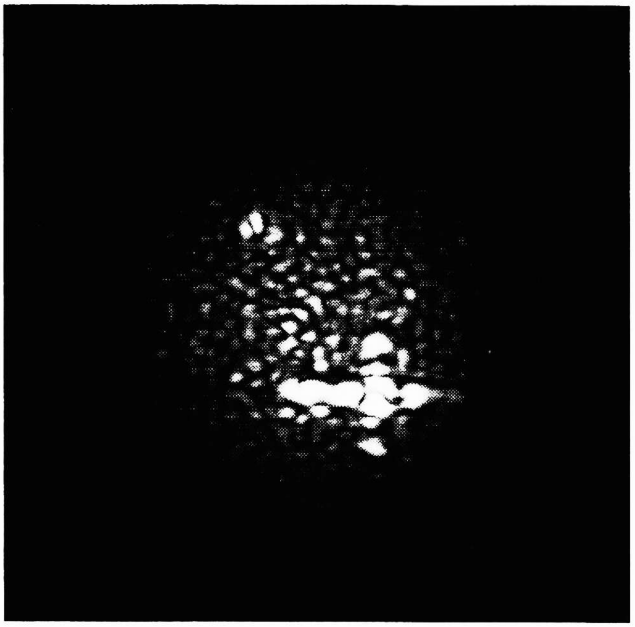

Figure 11. Reconstruction from experimentally collected data. The defect dimensions are shown in Figure 5 and their placement on the back side of the plate can be seen from the placement of the marker in Figure 4. The data for the reconstruction was collected at 253 kHz.

ACKNOWLEDGEMENTS

'he authors are grateful for support from the Institute for Manufacturing and Sustainment Technologies at The Pennsylvania tate University's Applied Research Laboratory. The Institute is a non-profit organization sponsored by the United States lavy Manufacturing Technology (MANTECH) Program, Office of Naval Research (contract number N00039-97-0042). ıny opinions, findings, conclusions or recommendations expressed in this material are those of the authors and do not ecessarily reflect the views of the U.S. Navy. The authors would also like to thank Dr. B. Bard for his assistance in securing quipment for the experiments, and for fruitful discussions.

REFERENCES

. J. W. Wagner, "Optical detection of ultrasound," in *Physical Acoustics, Principles and Methods*, **XIX**, pp. 201-265, Academic Press, New York, 1990.
. C. B. Scruby and L. E. Drain, *Laser Ultrasonics: Techniques and Applications*, Adam Hilger, Bristol, UK, 1990.
. J.-P. Monchalin, "Optical detection of ultrasound," *IEEE Trans. Ultrason. Ferroelec. Freq. Contr.*, **33**, pp. 485-499, 1986.

4. D. R. Bacon, "Primary calibration of ultrasonic hydrophones using optical interferometry," *IEEE Trans. Ultrason. Ferroelec. Freq. Contr.*, **35**, pp. 152-161, 1988.
5. R. Reibold and W. Molkenstruck, "Optical measuring techniques," in *Ultrasonic Exposimetry*, pp. 143-162, CRC Press, Boca Raton, 1993.
6. D. Royer and O. Casula, "Quantitative imaging of transient acoustic fields by optical heterodyne interferometry," *Proc. IEEE Ultrason. Sym.*, pp. 1153-1162, 1994.
7. J.-P. Monchalin, "Progress towards the application of laser-ultrasonics in industry," in *Review of Progress in QNDE*, **12**, pp. 495-506, Plenum Press, New York, 1993.
8. J.-P. Monchalin, C. Neron, and J. F. Bussiere, "Laser-ultrasonics: from the laboratory to the shop floor," *Phys. in Canada*, pp. 122-130, March/April 1995.
9. L. N. Tello, T. D. Black, D. P. Cudmore and R. Magnusson, "Characterization of ultrasonic transducers by means of double exposure holographic interferometry," *J. Acoust. Soc. Am.*, **101**, pp. 281-288, 1997.
10. B. Schneider and K. K. Shung, "Quantitative analysis of pulsed ultrasonic beam patterns using a Schlieren system", *IEEE Trans. Ultrason. Ferroelec. Freq. Contr.*, **43**, pp. 1181-1186, 1996.
11. J. W. Wagner, "Heterodyne holography for visulaization of surface acoustic waves," *Nondestr. Testing Commun.*, **2**, pp. 77-99, 1985.
12. J. W. Wagner, "High-resolution holographic techniques for visualization of surface acoustic waves," *Materials Evaluation*, **44**, pp. 1238-1243, 1984.
13. K.-J. Pohl, H.-A. Crostack and H. Meyer, "Holographic visualization of laser generated ultrasound for the detection and description of subsurface flaws," *Proc. SPIE*, **1756**, pp. 258-269, 1992.
14. C. Henning and D. Mewes, "Visualization of surface waves propagating over surfaces eroded due to particle impact," *Wear*, **186**, pp. 78-85, 1995.
15. K. Creath and J. C. Wyant, "Holographic and speckle testing," in *Optical Shop Testing*, 2nd ed., John Wiley & Sons, New York, 1992.
16. G. A. Gordon, B. A Bard, and S. Wu, "Wide-area imaging of ultrasonic fields by digital phase-stepping shearography," in *Review of Progress in QNDE*, **17A**, pp. 1729-1736, Plenum Press, New York, 1998.
17. B. A. Bard, G. A. Gordon and S. Wu, "Laser-modulated phase-stepped digital shearography for quantitative full-field imaging of ultrasonic waves," *J. Acoust. Soc. Am.*, **103**, pp. 3327-3335, 1998.
18. J.-C. Krapez, F. Taillade, T. Lamarque and D. Balageas, "Shearography: a tool for imaging Lamb waves in composites and their interaction with delaminations," to appear in *Review of Progress in QNDE*, **18**, Plenum Press, New York, 1999, accepted for publication.
19. C. Smith, "FAA inspection research - anticipating future inspection requirements, at http://www.asp.tc.faa.gov/FAATC/AAR430/techpapers/ATA_971.HTML
20. C. Smith, "Federal Aviation Administration aircraft inspection research and development programs," *Proc. SPIE*, **2945**, pp. 200-209, 1997.
21. J. L. Rose, K. Rajana and A. Pilarski, "Ultrasonic guided waves for NDE of adhesively bonded joints in aging aircraft," *Proc. Adhesion Soc.*, Feb. 20-24, Orlando, Fla., 1994.
22. A. Mal, Z. Chang, D. Guo, and M. Gorman, "Lap joint inspection using plate waves," *Proc. SPIE*, **2945**, pp. 128-137, 1997.
23. J. D. Achenbach, "Detection and characterization of cracks and corrosion in aging aircraft structures (part II)," *Key Eng. Mater.*, **145-149**, pp. 1149-1160, 1998.
24. K. J. Sun and P. H. Johnson, "Disbond detection in bonded aluminum joints using Lamb wave amplitude and time-of-flight," in *Review of Progress in QNDE*, (edited by D. O. Thompson and D. E. Chimenti), **13**, pp. 1507-1513, Plenum Press, New York, 1994.
25. Z. Chang and A. Mal, "A global-local method for wave propagation across a lap joint," AMD-Vol. **204**, *Numerical Methods in Structural Mechanics*, pp. 1-11, ASME, 1995.
26. G. A. Gordon and B. R. Tittmann, "Surface acoustic wave determination of subsurface structure," *NDTE*, **11**, pp. 21-32, 1994.
27. G. A. Gordon and B. R. Tittmann, "Surface elastic wave measurement for determination of steel hardness gradients," *Review of Progress in QNDE*, (edited by D. O. Thompson and D. E. Chimenti), **15,** pp. 1597-1604, Plenum Press, New York, 1996.
28. P. J. Torvik, "Reflection of wave trains in semi-infinite plates," *J. Acoust. Soc. Am.*, **41**, pp. 346-353, 1967.
29. R. D. Gregory and I. Gladwell, "The reflection of a symmetric Rayleigh-Lamb wave at the fixed edge of a plate," *J. Elast.*, **13**, pp. 185-206, 1983.
30. S. I. Rokhlin, "Lamb wave interaction with lap-shear adhesive joints: theory and experiment," *J. Acoust. Soc. Am.*, **89**,

pp. 2758-2765, 1991.
31. S. I. Rokhlin and F. Bendec, "Coupling of Lamb waves with the aperture between two elastic sheets," *J. Acoust. Soc. Am.*, **73**, pp. 55-60, 1983.
32. D. N. Alleyne and P. Cawley, "Interaction of Lamb waves with defects," *IEEE Trans. Ultras. Ferro. Freq. Contr.*, **39**, pp. 381-396, 1992.
33. Y. Cho, D. D. Hongerholt, and J. L. Rose, "Lamb wave scattering analysis for reflector characterization," *IEEE Trans. Ultrason. Ferroelec. Freq. Contr.*, **44**, pp. 44-52, 1997.
34. D. P. Jansen and D. A. Hutchins, "Ultrasonic Rayleigh and Lamb wave tomography," *Acustica*, **79**, pp. 117-127, 1993.
35. W. Wright, D. Hutchins, D. Jansen, and D. Schindel, "Air-coupled Lamb wave tomography," *IEEE Trans. Ultrason. Ferroelec. Freq. Contr.*, **44**, pp. 53-59, 1997.
36. J. C. P. McKeon and M. K. Hinders, ``Lamb wave contact scanning tomography,'' to appear in *Review of Progress in QNDE*, (edited by D. O. Thompson and D. E. Chimenti), **18**, pp. 1507-1513, Plenum Press, New York, 1999.
37. G. Lu, B. Bard, and S. Wu, "A real-time portable phase-stepping shearography system for NDE," *Proc. SPIE*, **3397**, pp. 156-167, 1998.
38. J. E. Greivenkamp and J. H. Bruning, "Phase shifting interferometry," Chapter 14, in *Optical Shop Testing*, ed D. Malacara, John Wileys and Sons Inc., New York, 1992.
39. R. Jones and C. Wykes, *Holographic and Speckle Interferometry*, Cambridge University Press, Cambridge, England, 1989.
40. I. A. Viktorov, Rayleigh and Lamb waves, Plenum Press, New York, 1967.
41. F. L. Degertekin and B. T. Kuri-Yakub, "Lamb wave excitation by Hertzian contacts with applications in NDE," *IEEE Trans. Ultrason. Ferroelec. Freq. Contr.*, **44**, pp. 769-778, 1997.
42. P. M. Morse and K. U. Ingard, *Theoretical Acoustics*, McGraw-Hill, New York, 1968.
43. A. J. Devaney, "A filtered backpropagation algorithm for diffraction tomography," *Ultrason. Imag.*, **4**, pp. 181-193, 1982.
44. T. D. Mast, A. I. Nachman, and R. C. Waag, "Focusing and imaging using eigenfunctions of the scattering operator," *J. Acoust. Soc. Am.*, **102**, pp. 715-725, 1997.
45. D. T. Borup, S. A. Johnson, W. W. Kim, and M. J. Berggren, "Nonperturbative diffraction tomography via Gauss-Newton iteration applied to the scattering integral equation," *Ultrason. Imag.*, **14**, pp. 69-85, 1992.
46. V. W. Sparrow and R. Raspet, "A numerical method for general finite amplitude wave propagation and its application to spark pulses," *J. Acoust. Soc. Am.*, **90**, pp. 2683-2691, 1991.
47. T. D. Mast, L. M. Hinkelman, M. J. Orr, V. W. Sparrow, and R. C. Waag, "Simulation of ultrasonic pulse propagation through the abdominal wall," *J. Acoust. Soc. Am.*, **102**, pp. 1177-1190, 1997.